Structural and Functional Characterization of a Biliverdin-Binding Near-Infrared Fluorescent Protein From the Serpin Superfamily

Manoilov, Kyrylo Yu.

2022-01-30

Manoilov , K Y , Ghosh , A , Almo , S C & V. Verkhusha , V 2022 , ' Structural and Functional Characterization of a Biliverdin-Binding Near-Infrared Fluorescent Protein From the Serpin Superfamily ' , Journal of Molecular Biology , vol. 434 , no. 2 , 167359 . https://doi.org/10.1016/j.jmb.2021.167359

http://hdl.handle.net/10138/351006
https://doi.org/10.1016/j.jmb.2021.167359

Journal Pre-proofs

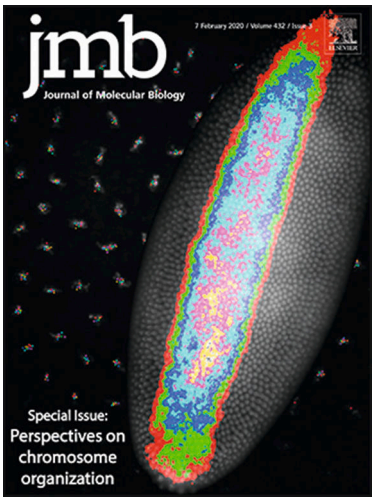

Fast Track

Structural and functional characterization of a biliverdin-binding near-infrared fluorescent protein from the serpin superfamily

Kyrylo Yu. Manoilov, Agnidipta Ghosh, Steven C. Almo, Vladislav V. Verkhusha

PII: S0022-2836(21)00596-9
DOI: https://doi.org/10.1016/j.jmb.2021.167359
Reference: YJMBI 167359

To appear in: *Journal of Molecular Biology*

Received Date: 18 September 2021
Revised Date: 6 November 2021
Accepted Date: 10 November 2021

Please cite this article as: K. Yu. Manoilov, A. Ghosh, S.C. Almo, V.V. Verkhusha, Structural and functional characterization of a biliverdin-binding near-infrared fluorescent protein from the serpin superfamily, *Journal of Molecular Biology* (2021), doi: https://doi.org/10.1016/j.jmb.2021.167359

Structural and functional characterization of a biliverdin-binding near-infrared fluorescent protein from the serpin superfamily

Kyrylo Yu. Manoilov[1], Agnidipta Ghosh[2], Steven C. Almo[2], and Vladislav V. Verkhusha[1,3,4,*]

[1]Departments of Anatomy and Structural Biology, and [2]Biochemistry, Albert Einstein College of Medicine, Bronx, NY 10461, U.S.A; [3]Medicum, Faculty of Medicine, University of Helsinki, Helsinki 00290, Finland; and [4]Science Center for Genetics and Life Sciences, Sirius University of Science and Technology, Sochi 354340, Russia

*Correspondence should be addressed to V.V.V. (vladislav.verkhusha@einsteinmed.org)

Abstract

Biliverdin-binding serpins (BBSs) are proteins that are responsible for coloration in amphibians and fluoresce in the near-infrared (NIR) spectral region. Here we produced the first functional recombinant BBS of the polka-dot treefrog *Boana punctata* (*Bp*BBS), assembled with its biliverdin (BV) chromophore, and report its biochemical and photochemical characterization. We determined the crystal structure of *Bp*BBS at 2.05 Å resolution, which demonstrated its structural homology to the mammalian protease inhibitor alpha-1-antitrypsin. BV interaction with *Bp*BBS was studied and it was found that the N-terminal polypeptide (residues 19–50) plays a critical role in the BV binding. By comparing *Bp*BBS with the available NIR fluorescent proteins and expressing it in mammalian cells, we demonstrated its potential as a NIR imaging probe. These results provide insight into the non-inhibitory function of serpins, provide a basis for improving their performance in mammalian cells, and suggest possible paths for the development of BBS-based fluorescent probes.

Keywords: biliprotein, phytochrome, tetrapyrrole, fluorescent protein, iRFP, Boana frog

Abbreviations: α1-AT, α1-antitrypsin; BBS, biliverdin-binding serpin; *Bp*BBS, biliverdin-binding serpin of *Boana punctata* treefrog; BV, biliverdin; NIR, near-infrared; FP, fluorescent protein; GuHCL, guanidine hydrochloride.

Introduction

Serpins (serine protease inhibitors) are among the most functionally diverse, but structurally conserved superfamily of proteins, the classical representatives of which play a role in inhibiting extracellular serine proteinases [1]. Inhibitory serpins share a similar mechanism of action, in which they form a stable covalent complex with a target proteinase. This process is typically accompanied by a remarkable structural rearrangement in the serpin secondary structure. However, a large group of serpins possesses atypical activities, such as inhibition of caspases [2] and cysteine proteinases [3], or various non-inhibitory functions, e.g., transport of low molecular weight compounds [4], molecular chaperone activity [5], or tumor suppression [6].

Recently, Taboada et al. [7] reported a novel group of serpins in frogs, which bind biliverdin (BV) and produce green coloration in some anuran species. BV is a linear tetrapyrrole, which is the enzymatic product of heme catabolism. The discovery of these BV-binding serpins (BBSs) provided the basis for fluorescence research in amphibians [8]. The presence of BBSs also accounts for the high levels of BV in organs and tissues of several taxonomic groups of amphibians. The latter property is referred to as 'physiological chlorosis'. In the species that exhibit physiological chlorosis, BV concentration in plasma is up to 200 fold higher than in the non-chlorotic ones [7]. Attempts to induce chlorosis in the non-chlorotic species by hemolysis or direct injection of BV have been unsuccessful, with the animals immediately excreting the excess BV [7]. The behavior suggests that in the context of a protein carrier complex, BV escapes excretion and accumulates in tissues.

Very little is known about the function of BBSs in anurans. Based on sequence analysis, one can predict that the closest known homologs of these proteins are the classical inhibitory serpins [7]. However, even if the inhibitory activity of these proteins is still preserved, their main function is to maintain the color of amphibians, which in itself is sufficient to include BBSs in the group of non-inhibitory serpins. Notably, non-inhibitory serpins provide unique opportunities for protein engineering and directed molecular evolution. Using these approaches, serpins of this group can be manipulated and repurposed for hormone transport [4] in the body. In addition, the study of BBSs will enhance our existing knowledge about functional diversity and evolution within the serpin superfamily.

One of the most important findings is that BBSs exhibit fluorescent properties analogous to bacteriophytochromes [9]. Hence these serpins have the potential to serve as templates for developing near-infrared (NIR) fluorescent proteins (FPs) [10]. The latter is especially relevant as NIR light can penetrate deep in mammalian tissues providing opportunities for deep-tissue imaging [11, 12].

Here, we obtained the first recombinant BBS of polka-dot treefrog *Boana punctata* (*Bp*BBS) in bacteria and characterized it *in vitro* and mammalian cells. We found that *Bp*BBS retains its ability to fluoresce when expressed in either bacterial or mammalian cells, which is a significant advantage over other natural FP-templates, which frequently do not fluoresce in mammalian cells without a preliminary modification [10, 13]. We also determined the crystal structure of *Bp*BBS, which reveals that *Bp*BBS is topologically similar to the members of the serpin superfamily and non-covalently binds BV. We demonstrate that the N-terminal region (residues 19–50) of *Bp*BBS plays a critical role in regulating fluorescence, likely, by affecting the interaction with the BV chromophore.

Results

Characterization of recombinant *Bp*BBS *in vitro*.

The *Bp*BBS sequence (residues 19–417) encoded by humanized codons and lacking secretion signal sequence was expressed in a TOP10 *E.coli* strain co-expressing heme oxygenase, which produces BV [14, 15]. The absorbance of the recombinant *Bp*BBS had a major peak at 648 nm, suggestive of efficient BV incorporation, and a minor peak at 386 nm corresponding to the Soret band (characteristic of most tetrapyrrole-binding proteins) (Figure 1 (A)). The spectra obtained for the recombinant protein are somewhat different from those reported for the purified glycosylated protein from frog lymph (390 nm and 667 nm, respectively [7]).

The fluorescence excitation maximum of *Bp*BBS peaked at 648 nm, and the maximum fluorescence emission was observed at 691 nm. The emission spectrum of *Bp*BBS is characterized by rapidly ascending left and gradually descending right slopes (Figure 1 (B)). This feature allows the protein to emit a significant amount of light in the near-infrared spectral range above 700 nm, which is potentially advantageous for deep-tissue imaging [16].

In size-exclusion chromatography, *Bp*BBS (14 mg/ml) eluted as a monodisperse peak (Suppl. Figure 1 (A)**)** indicating it is a monomer in solution, even at high concentrations. The molecular weight of the protein determined by SDS-PAGE (~50 kDa) (Suppl. Figure 1 (B)) is in good agreement with the predicted molecular weight of *Bp*BBS with hexahistidine tag (47.3 kDa). Fractions containing *Bp*BBS displayed the characteristic cyan color of BV-bound *Bp*BBS (Suppl. Figure 1 (C)).

The fluorescence quantum yield of *Bp*BBS is 0.3%, and the molecular extinction coefficient of *Bp*BBS is 44,200 M^{-1} cm^{-1}. These values were comparable to that of wild-type bacterial phytochromes, however, the quantum yield was substantially lower than that observed for the iteratively evolved NIR fluorescent proteins of the miRFP family [13]. Nevertheless, *Bp*BBS exhibited fluorescence maturation (appearance) kinetics comparable to miRFP670 and miRFP703, with a half-time of ~4.5 h (Figure 1 (C)). The pH stability of *Bp*BBS fluorescence was similar to or exceeded that for miRFP670 and miRFP703, resulting in the 50% fluorescence retention in the pH range of 5–10 (Figure 1 (D)). The pK_a of *Bp*BBS was 4.1 while most known NIR FPs have pK_a of 4.5 [13, 14, 16]. However, *Bp*BBS fluorescence was more susceptible to chaotropic agents, such as guanidine hydrochloride (GuHCl), than NIR FPs, retaining 50% of intensity after 20 min at 0.9 M GuHCl (Figure 2 (A)).

Incorporation of BV chromophore.

When expressed in an *E. coli* strain that does not produce BV, the *Bp*BBS apoprotein lacked the blue color characteristic of bound BV, and consequently lacked fluorescence. The apoprotein fully preserved its ability to bind BV as evidenced by the recovery of absorption and fluorescence properties after the addition of exogenous BV. Kinetic curves for BV binding (Figure 2 (B)**)** demonstrate the rapid reconstitution of the *Bp*BBS holoprotein with the rate [17] of 0.59 s^{-1}. Equilibrium BV titration (Figure 2 (C)) revealed the BV dissociation constant (K_d) of 2.7 μM.

The interaction of apoprotein and BV was non-covalent, as evidenced by the absence of a fluorescent band corresponding to *Bp*BBS in the zinc-induced fluorescence assay [18] in SDS-PAGE gel after treatment with Laemmli sample buffer containing 2-mercaptoethanol (Figure 2

(D)). In contrast, engineered from bacteriophytochromes miRFP proteins, which bind BV covalently via thioether linkage, exhibited the bright fluorescent bands.

Characterization of *Bp*BBS in mammalian cells.

The *Bp*BBS codon-optimized gene replaced EGFP in a pEGFP-N1 vector and was transiently transfected into the human HeLa cell line. *Bp*BBS fluorescence in HeLa cells detected by flow cytometry 48 h after transfection appeared to be ~24.7-fold higher than the autofluorescence background (Figure 3 (C)). The addition of exogenous BV to the cell culture medium increased the fluorescence level ~2.5-fold (Figure 3 (B, C)).

Fluorescence microscopy demonstrated that *Bp*BBS predominantly localized in the cell cytoplasm (~60–80%), with lower content in the cell nucleus (~20-40%) (Figure 3 (D)). In contrast, the cotransfected EGFP exhibited an equivalent or slightly lower cytoplasmic versus nuclear distribution. Because the molecular weight of *Bp*BBS is lower than the cut-off weight of passive transport through the nuclear pore (55-60 kDa), the predominant cytoplasmic localization suggests that *Bp*BBS either has an internal nuclear exclusion signal sequence or form a complex with some endogenous cytoplasmic protein.

*Bp*BBS is highly stable in mammalian cells. Incubation with bortezomib, an inhibitor of proteasome-dependent protein degradation, just slightly (~9%) increased its brightness (Figure 3 (E)). In contrast, upon bortezomib treatment the brightness of miRFP670 and miRFP720 [13] exhibited more pronounced enhancement (~20% and ~24%, respectively), indicating their lower cellular stability.

***Bp*BBS structure and comparison with α1-antitrypsin.**

Purified *Bp*BBS was crystallized using sparse matrix crystallization screens. Crystallization trials produced micro-crystals, which were further optimized with grid screening. After obtaining suitable crystals for diffraction analyses, a 2.05 Å X-ray dataset was collected. The crystals exhibit diffraction consistent with the primitive orthorhombic space group ($P2_12_12_1$; a = 72.1 Å, b = 75.9 Å, c = 143.8 Å) and contain two *Bp*BBS protomers in the asymmetric unit. The sequence closest to *Bp*BBS with a reported structure is human α1-antitrypsin (α1-AT) [7], and the *Bp*BBS structure was determined by molecular replacement using the coordinates of

uncleaved α1-AT (PDB ID: 1ATU) [19] as a search model. The final model contains a continuous polypeptide chain from residues 28–417 (Figure 4), expect residues 369–377 and exhibited excellent stereochemistry and geometry and refined to ideal R values (R_{work} / R_{free} = 20% / 23.7%; Table 1).

Notably, although *Bp*BBS shares only 46% sequence identity with human α1-AT (Suppl. Figure 2 (A)), the coordinates of *Bp*BBS and α1-AT superimpose with a root-mean-square deviation (RMSD) of 2.3 Å over 337 aligned Cα atoms (Suppl. Figure 2 (B)). The overall structure of *Bp*BBS exhibits a topology similar to that observed in uncleaved α1-AT, namely two near-orthogonally positioned central β sheets (sheet A and sheet B; Figure 4) surrounded by several α helices and β strands. Superimposition, however, highlighted several key differences between the two proteins (Suppl. Figure 2 and Suppl. Figure 3): (i) N-terminal polypeptide of *Bp*BBS is extended by 17 residues, which adopts a loop conformation, (ii) presence of BV in *Bp*BBS adjacent to sheet B, (iii) reorganization of *Bp*BBS segments encompassing residues 254–263 (β5–β6) and 278–308 (β7–α8) to accommodate BV (Suppl. Figure 3), and (iv) region 369–377 is disordered in *Bp*BBS; the analogous segment in α1-AT is a part of the reactive loop (Suppl. Figure 2 (A)).

BV chromophore and its environment.

Electron density is consistent with the non-covalent association of BV with the serpin-like polypeptide (Figure 5 (A)). Comparison of *Bp*BBS with miRFP670 and miRFP703 [13] reveals that the non-covalently bound BV adopts a distinct conformation (Figure 5 (B-D)). There are remarkable changes in torsional angles around the bonds between pyrrole rings A–B and C–D in *Bp*BBS. The torsional angle of the C5–C6 bond that joins ring A to ring B of the chromophore is rotated by ~108° compared to the chromophore of either miRFP670 or miRFP709 (Figure 5 (D)) [13]. Due to the change in the torsional angle, ring D is positioned almost orthogonal to the analogous rings of miRFP670 (~75°; Figure 5 (B)) and miRFP709 (~60°; Figure 5 (C)). The torsional changes are more pronounced around the C14–C15 bond, which bridges ring C and D. In *Bp*BBS the angle is 162°; however, the angles are -159° in both miRFP670 and miRFP703 (Figure 5 (E)). This torsional alteration places the pyrrole ring A of *Bp*BBS at about 35° to the ring A of miRFP670 and miRFP703, respectively (Figure 5 (B-D)). Therefore, BV adduct in the

miRFPs adopts the 5-Z,syn, 10-Z,syn, 15-Z,anti configuration (Figure 5 (F, G)), whereas in *Bp*BBS the BV molecule's configuration is all-Z, all-syn (Figure 5 (E)) [20].

The BV is engaged in polar interactions with the apoprotein (Figure 6 (A) and Suppl. Figure 4). The carboxyl group attached to ring C is H-bonded with the side chains of Thr265 and Arg300, and participates in a water-mediated H-bond interaction network with Glu273, Arg397, and Gln399. The ring nitrogen forms an H-bond with Ser296. The ring D is engaged in an H-bond network with the backbone nitrogen of Asn292 and the sidechain of Ser296. The carboxyl group of the pyrrole ring B is coordinated with the hydroxyl group of Tyr49 and sidechains of Arg293 and Gln399.

The bound chromophore is shielded from the solvent primarily by hydrophobic interactions provided by the *Bp*BBS sidechains (Figure 6 (B) and Suppl. Figure 4). Ring A of BV is inserted in an aromatic cleft created by the sidechains of Tyr64, Phe275, Leu291, Ile395, Phe396, Val409, and Gly410. Ring B is buttressed in the BV binding pocket of *Bp*BBS by sidechains of Ile5p7 and Phe61 on one side and Phe275 on the opposite side. Pyrrole ring C of BV is stabilized by π-π interaction with the Phe275 sidechain. In addition, Met303 provides a hydrophobic environment to ring C. Ring D of BV is stacked between the sidechains of Leu291 and Trp299. Furthermore, ring D is shielded from the solvent by sidechains of Met263, Leu287, Asn290, and Arg295. Ring D is additionally surrounded by the side chains of Leu287, Leu291, Asn292 and Arg295.

Mutations in N-terminal polypeptide.

Our structural analysis showed that the N-terminal polypeptide of *Bp*BBS interacts with BV or its immediate environment. To study its effect on *Bp*BBS fluorescence, we generated a series of N-terminal deletion variants (Suppl. Figure 5**)**. The N-terminally truncated *Bp*BBS variants almost completely lost the ability to fluoresce in bacteria (Suppl. Figure 5 (A)) and mammalian cells (Suppl. Figure 5 (B)). The truncations from N-terminal residues 19 to 27 had almost no effect on *Bp*BBS fluorescence. However, continued truncation at and beyond residue 30 resulted in a gradual decrease in fluorescence until levels comparable to autofluorescence were reached. The addition of exogenous BV to cells resulted in 2.5-4-fold increased fluorescence levels for the truncated *Bp*BBS variants, but the overall trend in the fluorescence reduction remained.

Moreover, the mutation of Tyr49 to Phe in the immediate environment of BV (Suppl. Figure 4) resulted in ~9-fold fluorescence decrease without exogenous BV and ~2-fold decrease when 25 μM BV was added (Suppl. Figure 5 (C)). Overall, these data suggested that the N-terminal polypeptide segment, in general, and Tyr49, in particular, play important roles in the recognition and binding of BV to *Bp*BBS.

Discussion

A few BV-binding proteins from vertebrates (animal biliproteins) have been characterized [21, 22]. *Bp*BBS is the first member of the recently discovered group of non-inhibitory BV-binding serpins (BBSs) found in anurans, which fluoresce in the NIR spectral range [7]. Our analysis of the major *Bp*BBS spectral and biochemical properties demonstrated their similarity with miRFPs engineered from bacteriophytochromes. *Bp*BBS exhibited a rather similar absorption, fluorescence excitation and emission spectra, molar extinction coefficient, fluorescence maturation rate, and pH stability (Figure 1), among others. However, its fluorescence quantum yield and fluorescence stability in GuHCl were substantially lower than for miRFPs (Figure 2 (A)), the latter was likely due to the non-covalent attachment of BV (Figure 2 (D)).

Other BBSs found in tropical frog species are homologous to *Bp*BBS [7]. Furthermore, several putative BBS–like anuran sequences predicted by BLAST alignment exhibit higher sequence similarity to *Bp*BBS than classical serpins, like α1-AT. These include *Hyla simplex* hylaserpin S1 (UniProt #H6SWK9), *Xenopus laevis* serpin domain-containing protein (UniProt #A0A1L8F9R6), and *X. tropicalis* serpin peptidase inhibitor (UniProt #A0A6I8SV03).

Protein engineering and directed molecular evolution approaches are very effective at enhancing and tuning protein properties, including fluorescence [10], and could be applied to BBS to develop new NIR FPs. BBSs from different frog species could also serve as molecular templates to develop distinct NIR FPs. Several *Bp*BBS properties suggest its suitability as a molecular template, including the monomeric state (Suppl. Figure 1 (A)) and high stability in mammalian cells (Figure 3 (E)).

Despite the similarity of optical properties of BBSs and bacteriophytochromes, our results indicate that the structure of these two groups of proteins is very different. We found that

*Bp*BBS has the polypeptide chain topology typical for the inhibitory representatives of serpins, like human α1-AT. Comparison of *Bp*BBS structure with those of non-inhibitory cofactor-bound serpins revealed that its BV-binding pocket is unique; and the protein regions forming the cofactor-binding sites in thyroxine- [23] and corticosteroid-binding [24] serpins are different. Compared to thyroxine and corticosteroids in complex with their respective apoproteins, BV is almost completely 'immersed' in the *Bp*BBS globule. The vinyl group of BV's D-ring is the only solvent-accessible segment. This observation suggests a possible structural rearrangement during the molecular cycle of the non-covalent BV binding and release from *Bp*BBS apoprotein.

In NIR FPs engineered from bacteriophytochromes, the $C3^2$ (or $C3^1$ in miRFP670) atom of ring A of BV forms a thioether bond with apoprotein Cys20 or Cys253 residue in miRFP703 or miRFP670, respectively [25], resulting in the reduction of the ring A and, consequently, decreased conjugation of the electron system of the formed BV-adduct (Figure 5). In addition, in wild-type bacteriophytochromes, ring D isomerizes between the *cis*- and *trans*-configurations via C15=C16 isomerization [26] upon light irradiation, which also modulates the degree of conjugation and, consequently, the absorption and fluorescence properties. We did not observe any light-induced changes in the *Bp*BBS spectra, indicating that the BV pyrrole rings do not change configuration upon illumination. Also, none of the BV rings in *Bp*BBS is reduced, retaining the same conjugation present in the unbound BV molecule. However, the *Bp*BBS spectra are more similar to that of the blue-shifted miRFP670 than to red-shifted miRFP720 [13]. We hypothesize that in *Bp*BBS, the low degree of conjugation between the rings A and B, and between C and D (Figure 5) decreases the electron conjugation system, which results in the blue-shifted than in unbound BV spectra.

Fluorescence quantum yield depends on the rigidity of the chromophore, which relies on its immediate environment and the formation of covalent attachments. The low quantum yield of *Bp*BBS fluorescence is most likely caused by non-radiative decay [10]. This is not surprising because absorption, not fluorescence, is important for BBS function in anurans, which is coloring camouflage. The BV pyrrole rings in *Bp*BBS are mainly stabilized by weak hydrophobic interactions with the polypeptide chain (Figure 6 and Suppl. Figure 4). Only a couple of polar interactions are observed involving rings C and D with Ser296 and Asn292, respectively. All other polar contacts are formed only with carboxyl groups of BV, which may not create any

obstacles to chromophore mobility. On the contrary, the BV pyrrole rings have a substantially larger number of polar bonds with the polypeptide in miRFPs [26].

The crystal structure reveals that the N-terminal polypeptide of *Bp*BBS (residues 28–50) is highly ordered and is in part stabilized by the serpin fold. In most structurally characterized serpins, the N-terminal polypeptide is disordered. The effect of the N-terminal polypeptide on *Bp*BBS fluorescence suggests its role in the regulation of BV binding and affinity. The observed interaction of the Tyr49 sidechain, which forms an H-bond with BV, highlights the connection between the N-terminal polypeptide and *Bp*BBS fluorescence.

In conclusion, our structural and functional characterization of the first NIR fluorescent *Bp*BBS serpin offers new insight into the biology of the serpin superfamily and provides the basis for the engineering of novel NIR FPs from BBSs found in tropical frogs.

Materials and Methods

Design of bacterial and mammalian plasmids. The gene encoding *Bp*BBS (UniProt #A0A7D7FB99) without secretion signal peptide (residues 19-417) was codon-optimized for expression in mammalian cells and synthesized by GenScript. For expression in mammalian cells, the *Bp*BBS gene was cloned between BglII and EcoRI sites in the backbone of pEGFP-N1 plasmid (Clontech) with EGFP gene removed by blunted BamHI-NotI sites. To produce *Bp*BBS in *E. coli*, the codon-optimized gene was inserted in the BglII and EcoRI sites of the pBAD/His-B vector (Invitrogen), which was previously modified [15] to minimize the linker between N-terminal hexahistidine tag and the gene (termed pBAD/His-D). Site-directed mutagenesis of *Bp*BBS was performed by overlap-extension polymerase chain reaction (PCR) [27]. Oligonucleotide PCR primers were purchased from Eurofins MWG Operon Oligos Tool (ThermoFisher Scientific). Plasmids encoding miRFP proteins for mammalian and bacterial expression have been described earlier [13].

Protein production in bacteria. *E.coli* TOP10 bacteria (Invitrogen) were cotransformed with pBAD/His-based vector encoding *Bp*BBS under arabinose promoter and by pWA23h vector encoding heme oxygenase (gene hmuO) from *Bradyrhizobium* strain ORS278 under the

rhamnose promoter [14, 15]. Cells were cultivated at 37°C with vigorous agitation (220 rpm) in LB medium containing 50 μg/ml kanamycin and 100 μg/ml ampicillin. For *Bp*BBS expression, 2 liters of fresh medium with 0.02% L-rhamnose in Erlenmeyer flask were inoculated with 50 ml of overnight *E. coli* culture and cultivated until OD_{600} of the cell suspension reached the value of 0.5–0.6. After that, *Bp*BBS expression was induced by the addition of 0.01% of L-arabinose. Expression was performed at 37°C for the first 6 h and then at 18°C overnight. The next day cells were pelleted by centrifugation upon 5,000 g for 15 min at 4°C (Sorvall RC5C Plus Refrigerated Centrifuge, Marshall Scientific) and resuspended in ice-cold phosphate buffered saline (PBS) with 10 mM imidazole and 10 mg/ml chicken egg white lysozyme. The cell suspension was incubated on ice for 10 min; thereafter, cells were disrupted by sonication (Model 3000 Ultrasonic Homogenizer; BioLogics) in a glass beaker in ice. The insoluble fraction of the cell homogenate was sedimented by centrifugation at 20,000g for 15 min and discarded.

Protein purification. The soluble fraction of the bacterial homogenate was applied to a Ni-NTA column, washed with PBS containing 10 mM imidazole, and the protein was eluted with 100 mM EDTA in PBS. A Superdex S200 (16/60) column equilibrated in 20 mM HEPES (pH 7.5), 150 mM NaCl, and 5 mM DTT was used to analyze the elution profile of *Bp*BBS. Under these buffer conditions, the column was calibrated with Gel Filtration Standard (Bio-Rad; catalog #151-1901) composed of thyroglobulin (MW 670 kDa), bovine γ-globulin (MW 158 kDa), chicken ovalbumin (MW 44 kDa), horse myoglobin (MW 17 kDa), and vitamin B12 (MW 1.35 kDa). The column flow was set to 1.5 ml/min.

SDS-PAGE characterization. A 10 μg solution of each protein was mixed 1:1 with 2x Laemmli sample buffer (62.5 mM Tris-HCl, pH 6.8, 2% SDS, 25% glycerol, 0.01% bromophenol blue) and heated at 100°C for 3 min. Thereafter, tubes with samples were centrifuged at 20,000g for 3 min and loaded in wells of precast polyacrylamide gels (Mini-PROTEAN TGX Gels; BioRad). Electrophoresis was run at 120 mW in Tris/Glycine Buffer (25 mM Tris, 192 mM glycine, 0.1% SDS, pH 8.3). Resulted gels were washed for 30 min in distilled water, fixed and stained in Coomassie G-250-containing solution (GelCode Blue Safe Protein stain, ThermoFisher Scientific).

Protein stability in GuHCl solution. A 5 µl aliquot of each protein containing the same molar concentration of the proteins was mixed with 120 µl of the GuHCl solutions of various concentrations. After 20 min incubation at room temperature, the fluorescence intensity was measured using a FluoroMax-3 spectrofluorimeter (Jobin Yvon) for each protein at the wavelengths corresponding to their excitation and emission maxima: ex. 648 nm, em. 691 nm for *Bp*BBS; ex. 642 nm, em. 670 nm for miRFP670; and ex. 674 nm, em. 703 nm for miRFP703).

Equilibrium BV titration. A 25 mg/ml stock solution of BV in DMSO was diluted in PBS and *Bp*BBS was added to obtain a series of BV concentrations from 0 to 10.44 µM with the constant concentration of *Bp*BBS (11.4 µM). Incubation was performed for 1 h at room temperature, and emission was recorded using a FluoroMax-3 spectrophotometer (Jobin Yvon).

Protein crystallization. Initial screening of *Bp*BBS was performed at concentrations of 0.340 mM (15 mg/ml) using 800 nl (protein:mother liquor = 1:1) sitting drops with a Crystal Gryphon (Art Robbins Instruments) utilizing MCSG (Microlytic) and PEG Ion HT (Hampton Research) sparse matrix crystallization suites. Crystals were eventually obtained in sitting drops by vapor diffusion against well solutions containing 0.2 M ammonium nitrate (pH 6.2) and 20% (w/v) PEG-3350 at 19 °C. For data collection, crystals were cryo-preserved by the addition of 12% ethylene glycol to the mother liquor before flash-cooling in liquid nitrogen.

Data collection, structure determination, refinement, and analysis. Data were collected with a Pixel Dectris Pilatus 6M detector, with a wavelength of 0.98 Å, on the ID-31 (LRL-CAT) beamline at the Argonne National Laboratory. Data from a single crystal were integrated and scaled using AIMLESS [28]. Diffraction from *Bp*BBS crystals was consistent with the orthorhombic space group $P2_12_12_1$ (a = 72.07, b = 75.9, c = 143.8) and extended to a resolution of 2.05 Å. Initial phases of crystals were determined by molecular replacement with PHASER [29] using refined coordinates of human α1-AT (PDB ID: 1ATU), as the search model. After determining the phases, an atomic model was built into the density using the automated model building program BUCCANEER [30] and manually inspected using COOT [31]. The model was

refined with REFMAC5 [32, 33] and PHENIX [34]. Analyses of the structures were performed in COOT [31] and MOLPROBITY [35]. The crystallographic model exhibited excellent geometry with no residues in disallowed regions of the Ramachandran plot [36]. Crystallographic statistics and RCSB accession codes are provided in Table 1.

Fluorescence macro-imaging. *E. coli* cotransformed with pWA23h plasmid and appropriate *Bp*BBS-encoding construct was streaked on a nitrocellulose membrane placed over LB agar Petri dish containing 50 μg/ml kanamycin and 100 μg/ml ampicillin, 0.02% L-rhamnose and 0.01% of L-arabinose. Thereafter, Petri dishes were incubated overnight at 37°C. The next day, an IVIS Spectrum imaging system was used for visualization of *Bp*BBS fluorescence in *E. coli* bacteria with fluorescence excitation wavelengths of 640 and 675 nm, and emission wavelengths of 700, 720, 740, 760, 780, and 800 nm.

Absorption and fluorescence spectroscopy. Absorbance spectra were measured using a Hitachi U-2000 spectrophotometer, and fluorescence excitation and emission spectra were recorded using a FluoroMax-3 spectrofluorimeter (Jobin Yvon). The molar extinction coefficient of *Bp*BBS was determined as the ratio of maximum absorbance of the main peak at the Q band and the minor peak at the Soret band, assuming that the extinction coefficient of the Soret band corresponds to 39,900 M^{-1} cm^{-1} [37]. The fluorescence quantum yield of *Bp*BBS was determined relative to that of Nile Blue dye in acidified ethanol with a known quantum yield of 0.27 [38].

Mammalian cell culture and cell transfection. HeLa cells were obtained from ATCC and were not additionally tested for mycoplasma. The cells were cultured in Dulbecco's Modified Eagle Medium (DMEM; HyClone) with 4 g/L glucose, 4 mM L-glutamine, 110 mg/L sodium pyruvate, and 100 μg/ml streptomycin and 100 IU penicillin G (Mediatech). Cell transfection was performed 48 h before initiation of experiments in 6-well or 12-well plates with an Effectene (Qiagen) or FuGENE (Promega) reagents. For microscopy, cells were cultured in 35 mm glass-bottom Petri dishes (Greiner Bio-One International). BV was added to cells 24 h before imaging. For fluorescence flow cytometry, the mammalian expression plasmid encoding *Bp*BBS was

cotransfected into HeLa cells with a plasmid encoding EGFP in 10:1 ratio. Then, the EGFP-positive cell populations were gated and their fluorescence in the NIR channel was analyzed. For protein degradation assays, cells were transfected with a plasmid expressing *Bp*BBS or miRFPs, and 4 h before flow cytometry, 10 μM of bortezomib was added.

Flow cytometry. 42 h after transfection with the appropriate plasmid constructs, live HeLa cells were washed with PBS and incubated in 10 mM of EDTA sodium salt solution in PBS at 37°C for 10-15 min. Then, 1% of BSA was added to the incubation solution, and cells were detached from the plastic surface by pipetting. The cell suspension was filtered through a 35 μm nylon mesh in round-bottom polystyrene tubes. Cell fluorescence intensity was analyzed with a BD LSRII flow cytometer. A 640 nm laser was used for *Bp*BBS excitation and various filter sets for analysis of emission: APC (650–685 nm), Alexa Fluor 700 (710–750 nm) and APC-Cy7 (750–810 nm). For analysis of EGFP fluorescence, a 488 nm blue laser was used for excitation and 500-575 nm filter set for emission. Minimally 3×10^5 cells were analyzed in each cell sample. Data were analyzed using a FACSDiva v.8.0.1 and a FlowJo v.7.6.2 software.

Fluorescence microscopy. Imaging of live HeLa cells was performed 48 h after transfection using an Olympus IX81 inverted microscope equipped with a 300 W xenon arc lamp (Sutter), a 60×1.35 numerical aperture (NA) oil objective lens (UPlanSApo, Olympus), and an Orca CCD camera (Hitachi). Chroma Cy5.5 (HQ665/45x, HQ725/50m, Q695LP) filter set was used to acquire NIR fluorescence and FITC (HQ480/40x, HQ530/40m, 505DCXR) filter set was used to acquire green fluorescence. During imaging, HeLa cells were incubated in a cell imaging medium (Life Technologies-Invitrogen) and kept at 35 °C. The microscope was operated with a SlideBook v.6.0.8 software (Intelligent Imaging Innovations).

Data Availability

The main data supporting the findings of this study are available within the article and its **Supplementary Information**. Additional data are available from the corresponding author. The *Bp*BBS structural data were deposited at the Protein Data Bank (PDB ID: 7RBW)

Acknowledgments

We thank E. Fedorov for the help with *Bp*BBS purification and crystallization, and O. Oliinyk for the valuable suggestions. This work was supported by the grants GM122567 and CA198095 from the U.S. National Institutes of Health, 322226 from the Academy of Finland, and 21-64-00025 from the Russian Science Foundation. K.Yu.M. was fully supported by the GM122567 grant.

Competing Interest Statement

The authors declare no competing interests.

Author Contributions

K.Yu.M. characterized *Bp*BBS *in vitro* and mammalian cells. A.G. and S.C.A. crystallized and determined *Bp*BBS structure. V.V.V. planned and directed the project and together with all authors designed the experiments, analyzed the data, and wrote the manuscript.

Additional information

Supplementary Information is available online.

Table 1. Crystallographic data statistics.

Data Collection*	
Source	APS ID-31
Wavelength (Å)	0.98
Number of crystals	1
Space group	$P2_12_12_1$
Cell dimensions	
a,b,c (Å)	72.1, 75.9, 143.8
Resolution (Å)	20-2.05 (2.123-2.05)
Completeness (%)	99.7 (99.8)
Total reflections	643967
Unique reflections	50138
Wilson B-factor	37.5
Multiplicity	12.8 (13.1)
R_{merge} (%)	8.5 (78.3)
$CC_{1/2}$ (%)	99.9 (92.2)
CC* (%)	100 (97.9)
<I>/s(I)	18.1 (4.7)
Refinement*	
Reflections: work/free	50072 (2595)/2481 (128)
R_{work}/R_{free} (%)	20.0 (24.6)/23.7 (27.3)
Number of TLS groups	11
Number of atoms	
Protein	6174
Ligand	86
Water	134
Average B-factors (Å^2)	
Protein	52.2
Ligand	33.4
Water	41.7
r.m.s.d.	
Bond lengths (Å)	0.003
Bond angles (°)	0.7
Molprobity †	
Favored	97.3% (739 a.a.)
Allowed	100% (760 a.a.)
Outliers	none
Clash score	100th percentile
Molprobity score	100th percentile

* Statistics calculated using PHENIX [34], highest resolution shells indicated in parentheses.
† Calculated with the program MOLPROBITY [35].

Figure legends

Figure 1. Characterization of recombinant purified *Bp*BBS protein. (A**)** Absorption spectrum of *Bp*BBS. (B) Fluorescence excitation and emission spectra of *Bp*BBS. (C) Kinetics of maturation of *Bp*BBS, miRFP670, and miRFP703 in *E. coli*. Time '0' corresponds to the beginning of the 1-h-long pulse-chase induction of the protein expression. (D) pH dependencies of NIR fluorescence for *Bp*BBS, miRFP670, and miRFP703.

Figure 2. Comparison of *Bp*BBS protein with selected NIR FPs. (A) Stability of *Bp*BBS, miRFP670, and miRFP703 after 20 min incubation in the GuHCl solutions. (B) Kinetics of BV binding by *Bp*BBS apoprotein. (C) Equilibrium BV titration of *Bp*BBS apoprotein. (D) SDS-PAGE and zinc-induced fluorescence of *Bp*BBS, miRFP670, miRFP703, and miRFP720. Protein staining is Coomassie G-250 staining.

Figure 3. Characterization of *Bp*BBS protein in human HeLa cells. A. Flow cytometry of *Bp*BBS without the addition of exogenous biliverdin (no BV) to cell culture medium: mock-transfected control cells and *Bp*BBS expressing cells. (B) Flow cytometry of *Bp*BBS with exogenously added BV (25 μM) to cell culture medium: mock-transfected control cells and *Bp*BBS expressing cells. In A and B, 10^5 cells were analyzed in each sample. (C) Comparison of cell brightness of the control and *Bp*BBS-expressing cells with and without BV presented in panels A and B. (D) Fluorescence images of cells expressing *Bp*BBS without and with (25 μM) exogenously added BV in cell culture medium. *Bp*BBS was imaged in Cy5.5 channel and EGFP in FITC channel. Scale bar is 20 μm. (E) Fluorescence of cells expressing *Bp*BBS, miRFP670, and miRFP720: non-treated and after 4 h incubation with 10 μM bortezomib.

Figure 4. Structure of *Bp*BBS highlighting biliverdin (BV) binding site. View of the *Bp*BBS monomer shown in ribbon representation (colored blue) with secondary structure elements indicated by arrows (β strands) and ribbons (helices). Serpin-specific two central β sheets are indicated. The bound BV is shown in stick representation (colored magenta) and labeled. A

disordered segment in *Bp*BBS is shown by spaced line (–). N and C denote the location of the N- and C-termini, respectively.

Figure 5. Structure and comparison of bound biliverdin to *Bp*BBS. (A) Views of composite omit maps (5% omission of the coordinates, contoured at 1.5σ; blue mesh) around biliverdin (BV) chromophore. (B) Overlay of BV in *Bp*BBS and BV-adduct in miRFP670 (stick representation with Cys20 adduct; yellow) structures highlights a distinct conformation of BV in *Bp*BBS. Pyrrole rings A and D and differences in their angle planes are denoted to emphasize the relative orientation of the rings in *Bp*BBS and miRFP670. (C) Overlay of BV in *Bp*BBS and BV-adduct in miRFP703 (with Cys253 adduct; cyan) as described in panel B. (D) Observed torsional angles between the pyrrole rings A and B or C and D in *Bp*BBS, miRFP670, and miRFP703. (E) Chemical structure of BV bound to *Bp*BBS highlights individual pyrrole rings and selected carbon atoms around them. (F) Chemical structure of BV-adduct in miRFP670 (as in panel E). (G) Chemical structure of BV-adduct in miRFP703 (as in panel E).

Figure 6. A close-up view of interactions of *Bp*BBS with biliverdin (BV). (A) The sidechains (color-coded as in Figure 4) of *Bp*BBS involved in polar interactions (black dashed line) with BV (magenta) are shown in stick representation. Water molecules are denoted in red spheres. Potential atomic contacts are indicated by dashed lines. (B) Views of the *Bp*BBS sidechains (as in panel A) that participate in hydrophobic interactions with BV (as in panel A).

References

[1] Law RH, Zhang Q, McGowan S, Buckle AM, Silverman GA, Wong W, et al. An overview of the serpin superfamily. Genome Biol. 2006;7:216.

[2] Suraweera CD, Hinds MG, Kvansakul M. Poxviral Strategies to Overcome Host Cell Apoptosis. Pathogens. 2020;10.

[3] Tušar L, Usenik A, Turk B, Turk D. Mechanisms Applied by Protein Inhibitors to Inhibit Cysteine Proteases. Int J Mol Sci. 2021;22.

[4] Carrell RW, Read RJ. How serpins transport hormones and regulate their release. Semin Cell Dev Biol. 2017;62:133-41.

[5] Ito S, Nagata K. Biology of Hsp47 (Serpin H1), a collagen-specific molecular chaperone. Semin Cell Dev Biol. 2017;62:142-51.

[6] Bodenstine TM, Seftor RE, Khalkhali-Ellis Z, Seftor EA, Pemberton PA, Hendrix MJ. Maspin: molecular mechanisms and therapeutic implications. Cancer Metastasis Rev. 2012;31:529-51.

[7] Taboada C, Brunetti AE, Lyra ML, Fitak RR, Faigón Soverna A, Ron SR, et al. Multiple origins of green coloration in frogs mediated by a novel biliverdin-binding serpin. Proc Natl Acad Sci U S A. 2020;117:18574-81.

[8] Taboada C, Brunetti AE, Pedron FN, Carnevale Neto F, Estrin DA, Bari SE, et al. Naturally occurring fluorescence in frogs. Proc Natl Acad Sci U S A. 2017;114:3672-7.

[9] Chernov KG, Redchuk TA, Omelina ES, Verkhusha VV. Near-Infrared Fluorescent Proteins, Biosensors, and Optogenetic Tools Engineered from Phytochromes. Chem Rev. 2017;117:6423-46.

[10] Oliinyk OS, Chernov KG, Verkhusha VV. Bacterial Phytochromes, Cyanobacteriochromes and Allophycocyanins as a Source of Near-Infrared Fluorescent Probes. Int J Mol Sci. 2017;18.

[11] Kaberniuk AA, Shemetov AA, Verkhusha VV. A bacterial phytochrome-based optogenetic system controllable with near-infrared light. Nat Methods. 2016;13:591-7.

[12] Fomicheva A, Zhou C, Sun QQ, Gomelsky M. Engineering Adenylate Cyclase Activated by Near-Infrared Window Light for Mammalian Optogenetic Applications. ACS Synth Biol. 2019;8:1314-24.

[13] Matlashov ME, Shcherbakova DM, Alvelid J, Baloban M, Pennacchietti F, Shemetov AA, et al. A set of monomeric near-infrared fluorescent proteins for multicolor imaging across scales. Nat Commun. 2020;11:239.

[14] Shcherbakova DM, Verkhusha VV. Near-infrared fluorescent proteins for multicolor in vivo imaging. Nat Methods. 2013;10:751-4.

[15] Piatkevich KD, Subach FV, Verkhusha VV. Far-red light photoactivatable near-infrared fluorescent proteins engineered from a bacterial phytochrome. Nat Commun. 2013;4:2153.

[16] Shcherbakova DM, Stepanenko OV, Turoverov KK, Verkhusha VV. Near-Infrared Fluorescent Proteins: Multiplexing and Optogenetics across Scales. Trends Biotechnol. 2018;36:1230-43.

[17] Jarmoskaite I, AlSadhan I, Vaidyanathan PP, Herschlag D. How to measure and evaluate binding affinities. Elife. 2020;9.

[18] Narikawa R, Nakajima T, Aono Y, Fushimi K, Enomoto G, Ni Ni W, et al. A biliverdin-binding cyanobacteriochrome from the chlorophyll d-bearing cyanobacterium Acaryochloris marina. Sci Rep. 2015;5:7950.

[19] Ryu SE, Choi HJ, Kwon KS, Lee KN, Yu MH. The native strains in the hydrophobic core and flexible reactive loop of a serine protease inhibitor: crystal structure of an uncleaved alpha1-antitrypsin at 2.7 A. Structure. 1996;4:1181-92.

[20] Bandara S, Rockwell N, Zeng X, Ren Z, Wang C, Shin H, et al. Molecular Basis of Far-red Sensing in Cyanobacteriochrome. bioRxiv. 2020:2020.06.02.130930.

[21] Ghosh S, Yu CL, Ferraro DJ, Sudha S, Pal SK, Schaefer WF, et al. Blue protein with red fluorescence. Proc Natl Acad Sci U S A. 2016;113:11513-8.

[22] Manjunatha GKS, Peter A, Naika MBN, Niranjana P, Shamprasad P. Identification of In-Vitro Red Fluorescent Protein with Antipathogenic Activity from the Midgut of the Silkworm (Bombyx Mori L.). Protein Pept Lett. 2018;25:302-13.

[23] Zhou A, Wei Z, Read RJ, Carrell RW. Structural mechanism for the carriage and release of thyroxine in the blood. Proc Natl Acad Sci U S A. 2006;103:13321-6.

[24] Klieber MA, Underhill C, Hammond GL, Muller YA. Corticosteroid-binding globulin, a structural basis for steroid transport and proteinase-triggered release. J Biol Chem. 2007;282:29594-603.

[25] Baloban M, Shcherbakova DM, Pletnev S, Pletnev VZ, Lagarias JC, Verkhusha VV. Designing brighter near-infrared fluorescent proteins: insights from structural and biochemical studies. Chem Sci. 2017;8:4546-57.

[26] Shcherbakova DM, Baloban M, Pletnev S, Malashkevich VN, Xiao H, Dauter Z, et al. Molecular Basis of Spectral Diversity in Near-Infrared Phytochrome-Based Fluorescent Proteins. Chem Biol. 2015;22:1540-51.

[27] Hilgarth RS, Lanigan TM. Optimization of overlap extension PCR for efficient transgene construction. MethodsX. 2020;7:100759.

[28] Winn MD, Ballard CC, Cowtan KD, Dodson EJ, Emsley P, Evans PR, et al. Overview of the CCP4 suite and current developments. Acta Crystallogr D Biol Crystallogr. 2011;67:235-42.

[29] McCoy AJ, Grosse-Kunstleve RW, Adams PD, Winn MD, Storoni LC, Read RJ. Phaser crystallographic software. J Appl Crystallogr. 2007;40:658-74.

[30] Cowtan K. The Buccaneer software for automated model building. 1. Tracing protein chains. Acta Crystallogr D Biol Crystallogr. 2006;62:1002-11.

[31] Emsley P, Cowtan K. Coot: model-building tools for molecular graphics. Acta Crystallogr D Biol Crystallogr. 2004;60:2126-32.

[32] CCP4. The CCP4 suite: programs for protein crystallography. Acta Crystallogr D Biol Crystallogr. 1994;50:760-3.

[33] Murshudov GN, Skubák P, Lebedev AA, Pannu NS, Steiner RA, Nicholls RA, et al. REFMAC5 for the refinement of macromolecular crystal structures. Acta Crystallogr D Biol Crystallogr. 2011;67:355-67.

[34] Liebschner D, Afonine PV, Baker ML, Bunkóczi G, Chen VB, Croll TI, et al. Macromolecular structure determination using X-rays, neutrons and electrons: recent developments in Phenix. Acta Crystallogr D Struct Biol. 2019;75:861-77.

[35] Chen VB, Arendall WB, 3rd, Headd JJ, Keedy DA, Immormino RM, Kapral GJ, et al. MolProbity: all-atom structure validation for macromolecular crystallography. Acta Crystallogr D Biol Crystallogr. 2010;66:12-21.

[36] Ramachandran GN, Ramakrishnan C, Sasisekharan V. Stereochemistry of polypeptide chain configurations. J Mol Biol. 1963;7:95-9.

[37] Filonov GS, Piatkevich KD, Ting LM, Zhang J, Kim K, Verkhusha VV. Bright and stable near-infrared fluorescent protein for in vivo imaging. Nat Biotechnol. 2011;29:757-61.

[38] Sens R, Drexhage KH. Fluorescence quantum yield of oxazine and carbazine laser dyes. Journal of Luminescence. 1981;24-25:709-12.

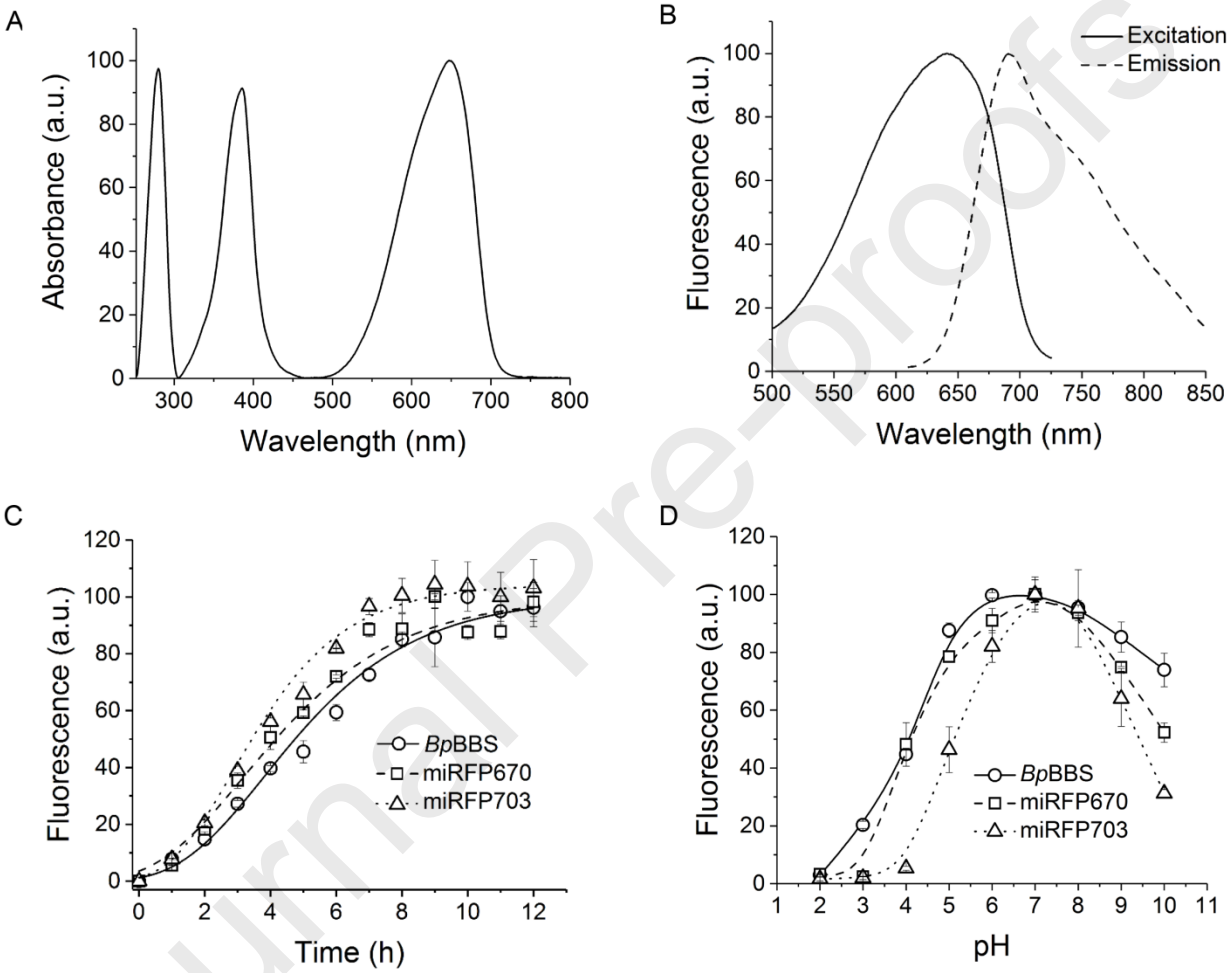

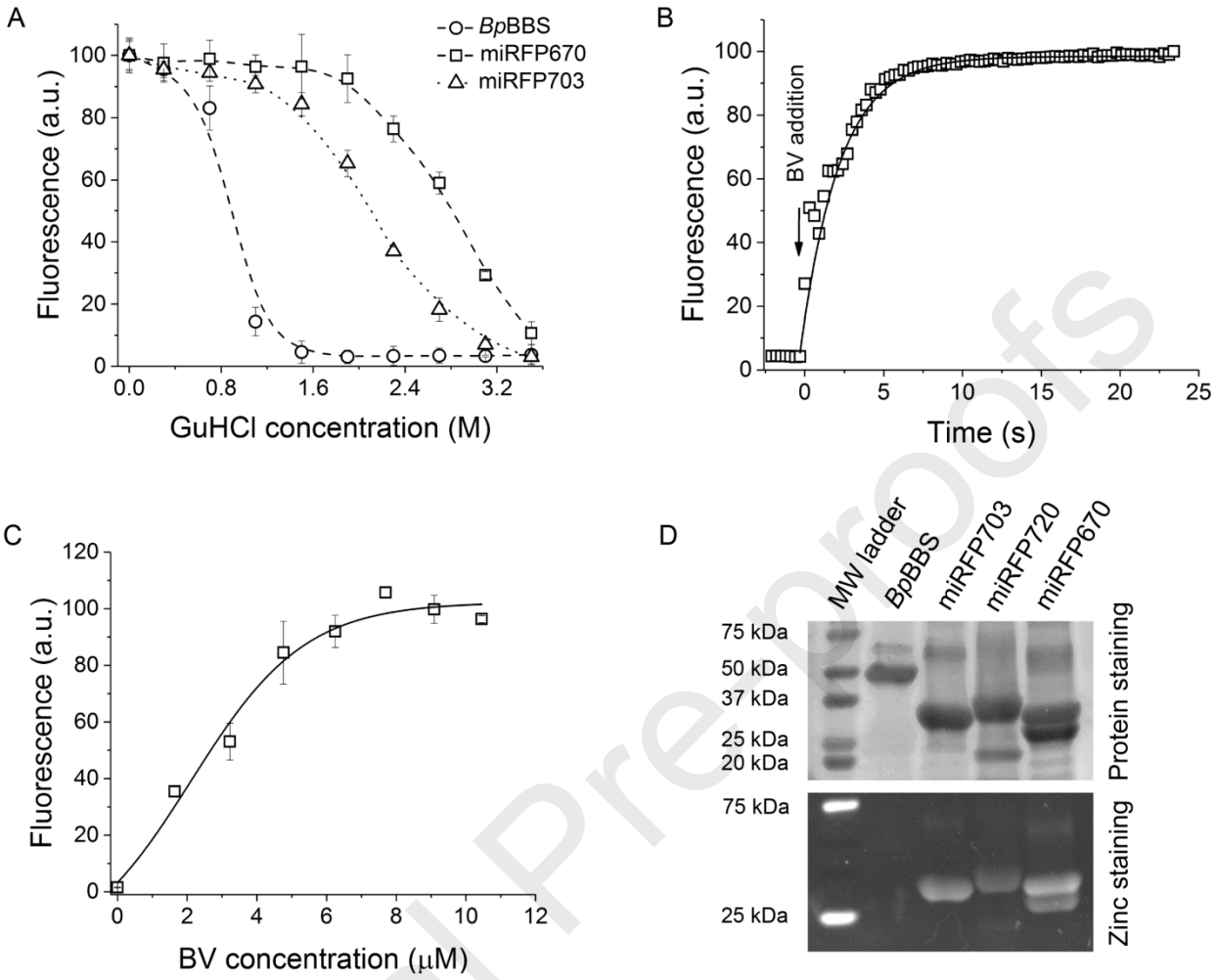

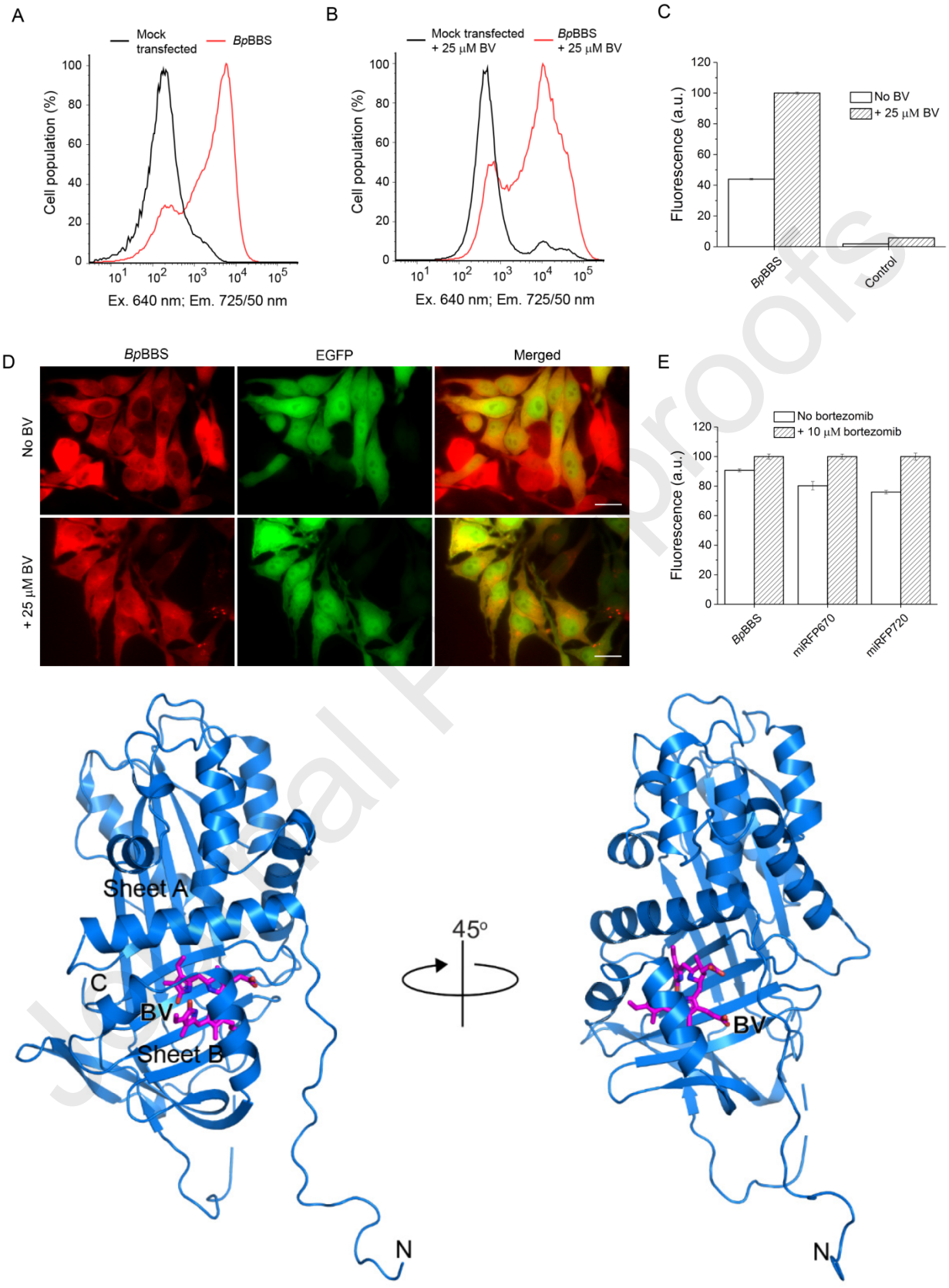

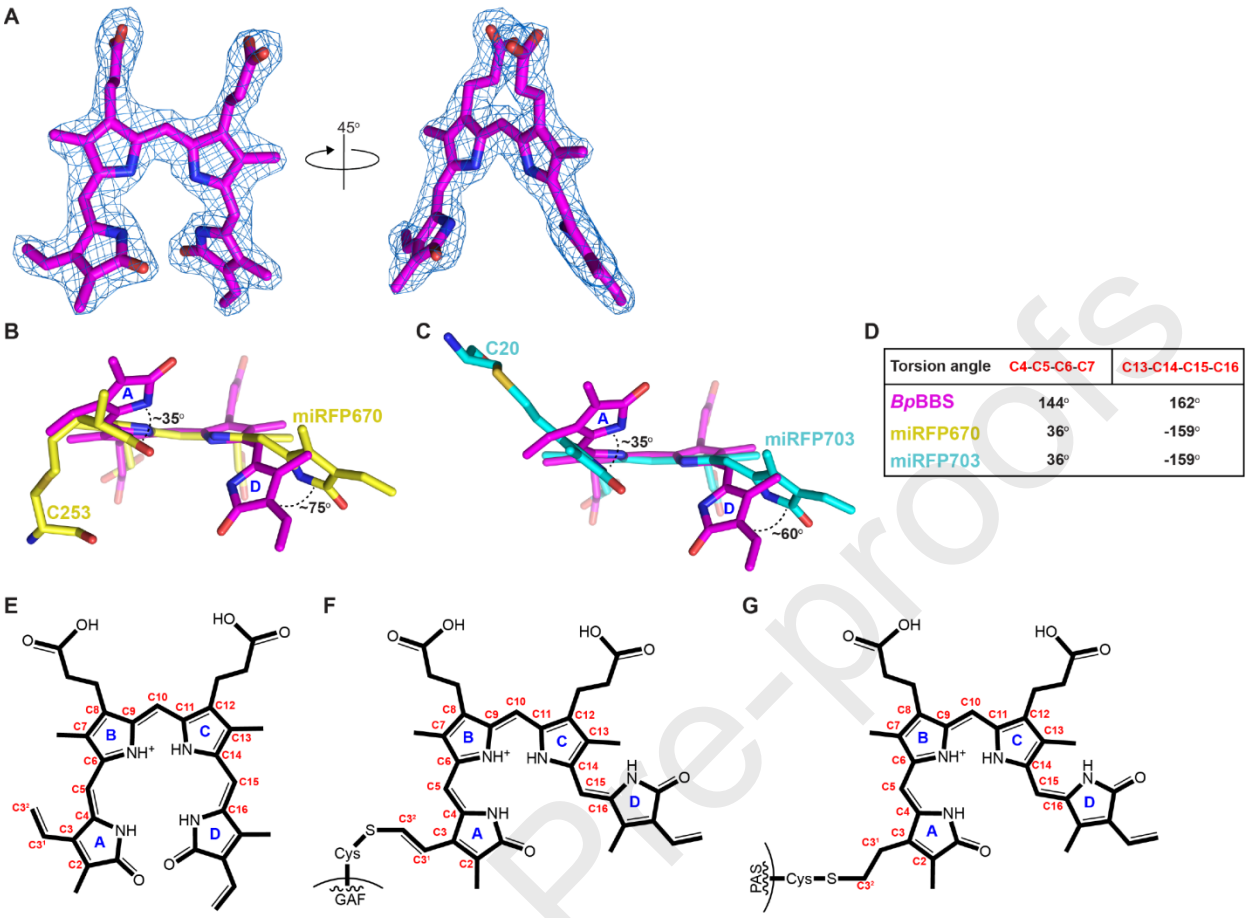

Torsion angle	C4-C5-C6-C7	C13-C14-C15-C16
*Bp*BBS	144°	162°
miRFP670	36°	-159°
miRFP703	36°	-159°

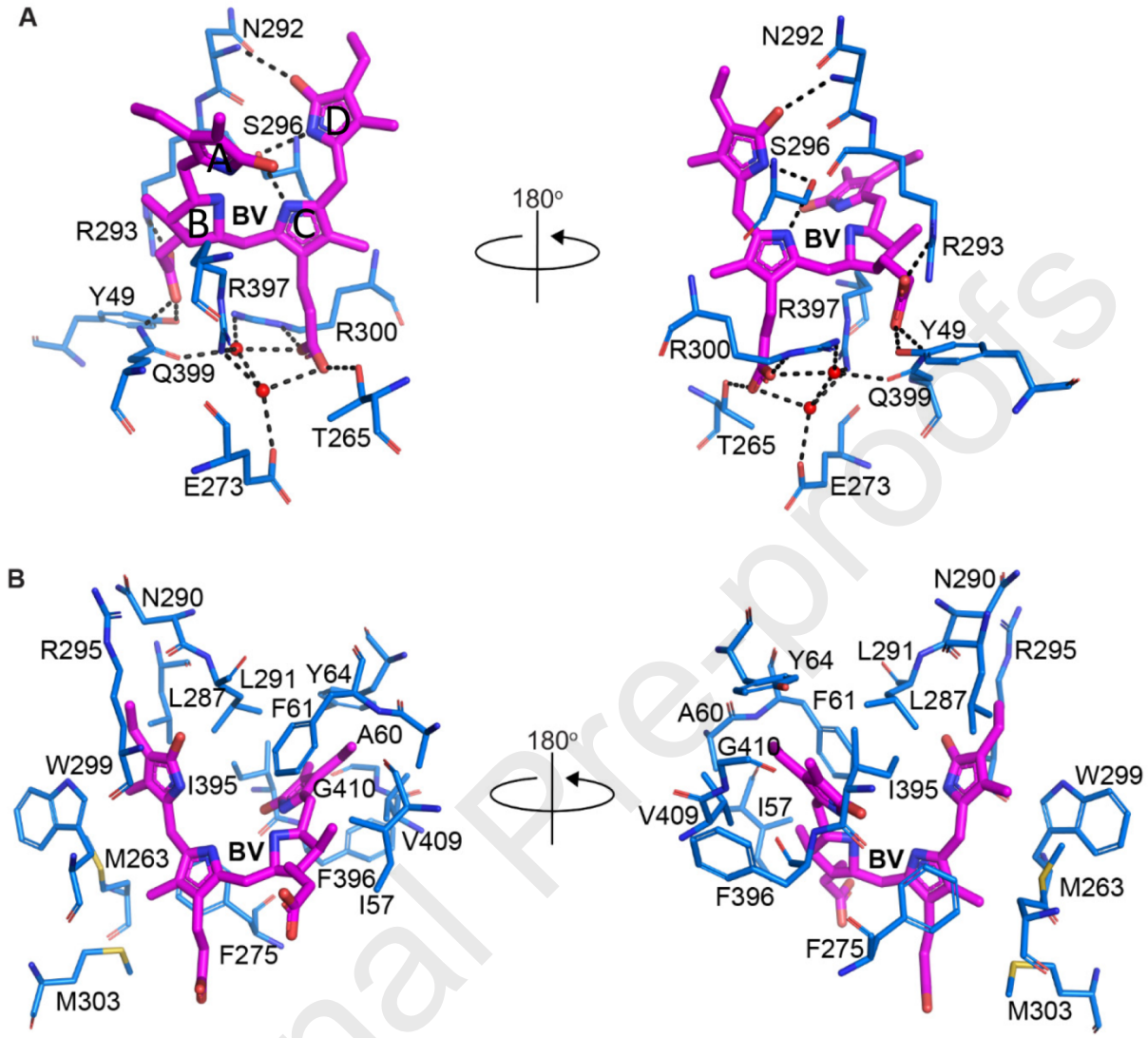

CRediT author statement

K.Yu.M. characterized *Bp*BBS *in vitro* and mammalian cells. A.G. and S.C.A. crystallized and determined *Bp*BBS structure. V.V.V. planned and directed the project and together with all authors designed the experiments, analyzed the data, and wrote the manuscript.

Declaration of interest

The authors declare no competing interests.

Graphical abstract